ORIGINAL ARTICLE

Frequency properties of acoustic emissions from the dry and saturated rock

Xiangxin Liu[1,2] · Lixin Wu[3] · Yanbo Zhang[2] · Zhengzhao Liang[4] · Xulong Yao[2] · Peng Liang[2]

Abstract

Different frequency bands (FBs) of acoustic emission (AE) signals from rock fractures contain diverse information about the physical and mechanical properties of a rock. This study proposes a frequency division processing method for the standard description expressions of discrete signals and for defining the integrated characteristics of AE signals. The frequency evolution of rock fracture-related AEs was investigated under uniaxial loading conditions, and rocks in dry and saturated states were examined and compared using AE information in FBs. The correlation between the water state and FBs of AE signal was addressed. The FB features (e.g., energy concentration) were analyzed, and their changes in water conditions were also considered by focusing on the FBs with the greatest energy concentrations. During rock fracturing, dry and saturated samples developed various shear-tensile damage patterns or "rock bridge" modes. The moisture property of rock affected the peak strength, plastic deformation, and intensity of the rock destruction, and the statistical relationship observed between rise time/ amplitude and average frequency showed that the crack characteristics depended on the presence or absence of moisture. The most suitable FB to distinguish the water state was 31.25–62.5 kHz. The parameter ζ (i.e., variable energy coefficient) exhibited a sudden increase in the FB of 0–31.25 kHz. This rapid change was more remarkable than that in the other FBs. This FB should be considered useful for monitoring to help predict the final rupture. The method developed here provides a new way for examining the rock damage characteristics and discovering the fracturing behavior patterns.

Keywords Rock fracturing · Saturated · Dry · Acoustic emission · Frequency band

Introduction

Rock damage by rupture is a process in which internal cracks are initiated, then extended, and finally joined, thus breaking the rock. Cracks can vary in size from micro-scale to macro-scale (Scholz 1968; Kranz 1983; Yangidani et al. 1985; Tang 1997; Wu et al. 2000; He et al. 2010). The acoustic emission (AE) phenomenon is defined as elastic waves associated with a rapid release of localized stress energy that is propagated with a material. AE has been proven to be a useful tool for investigating rock fractures (Lavrov 2003; Liu et al. 2015; Li et al. 2017). Various researchers have studied AE monitoring to understand rock mechanics and fracturing.

AE or micro-seismic (MS) characteristics were initially considered part of earthquake research. When increasing stress was applied to various brittle materials, elastic shocks (AE signals) began to occur at some stress states and increased generally with stress. They occurred further frequently with the increasing degree of heterogeneity (Mogi 1962). The experiment was monitored with an array of transducers around a sample to permit the full-waveform capture, location, and analysis of MS events for understanding the physical processes that generate seismicity within volcanic edifices. Basalt from Mount Etna (Italy) was selected as the rock sample (Benson et al. 2008). Then, strong similarities were observed between the small quakes that follow main earthquakes (the so-called aftershock sequence) and the AE

✉ Xiangxin Liu
   liuxiangxin9@163.com

✉ Lixin Wu
   awulixin@263.net

1 School of Resources and Civil Engineering, Northeastern University, Shenyang 110819, China

2 College of Mining Engineering, North China University of Science and Technology, Tangshan 063210, China

3 School of Geosciences and Info-physics, Central South University, Changsha 410083, China

4 School of Civil Engineering, Dalian University of Technology, Dalian 116024, China

activity that follows sample fracturing. The spectrograms of natural and laboratory seismicity were similar once allowance was provided for the different frequencies. They inferred that the evolution of the seismic signal with time was similar, suggesting that the underlying physical process was the same (Burlini and Toro 2008).

Researchers proposed that different fracture mechanisms generated different AE signals. The failure process of fractured marble was locally progressive, and the AE event accumulation was strongly related to the loading process and stress redistribution in rock. Natural fractures were widely distributed among rocks, and the spatial evolutions of different natural fractures could be successfully located and tracked by AE information (Enomoto and Hashimoto 1990; Pei et al. 2016). A signal-processing method inspired by a musical staff was proposed to describe the AE signal comprehensively. The processed information required a small storage space to maintain high fidelity (Zheng and Wu 2015). The cracking levels were detected through the parametric analysis of AE signals, thereby correlating these parameters to stress–strain plots of rocks. The number of AE hits was related to the number of cracks, and the AE energy was related to the magnitude of the cracking event (Moradian et al. 2016). The AE patterns triggered by stress level, loading time, and loading history were discussed and summarized. A damage variable based on AE parameters and a methodology for its determination were established. The rock fracturing evolution was quantified by AE information combined with other monitoring equipment (Chen and Yu 1984; Wieser et al. 2015; Zhang et al. 2015; Rodríguez et al. 2016; Wang et al. 2016; Meng et al. 2016).

An analysis of continuous waveforms from 40 to 60 dB channels demonstrated a wide range of waveform amplitudes for investigating the influences of AE equipment parameter settings on the monitoring effect. Two regimes of fracturing (nucleation and quasi-static fault propagation and dynamic fault propagation) were identified, and their AE characteristics were discussed and investigated (Goodfellow et al. 2014). Various rupture modes of rock damage can be identified by complex frequency components. Certain characteristics of AE signals can be captured before rock burst occurs. The continuous waveform of low-frequency and high-amplitude values was closely related to rock burst occurrences. H-type waveforms with high dominant frequencies were caused by shear failure, and L-type waveforms with low dominant frequency were produced by tension failure (Jia 2013; He et al. 2015; Li et al. 2017). The beginning of rock rupture was characterized by an increase in the high-frequency components of AE signals. A high frequency of AE components has been identified in some situations, whereas a low frequency of AE components can indicate an imminent rock burst (Armstrong 1969; Calder and Madsen 1989; Lu et al. 2012).

Several characteristic parameters were extracted as discriminant indicators to distinguish between the seismic events and blasts that generate seismic waveforms. Fisher classifier, naive Bayesian classifier, and logistic regression were used to establish the discriminators between seismic events and blasts. Research results showed a reasonably good discriminating performance (Dong et al. 2016a, b, 2017). A modification of the original AE *b* value is proposed on the basis of the use of AE energy signals. The evolution of the energy *b* value indicates the onset of severe damage (Sagasta et al. 2018).

The results of these studies have been used to apply the AE technology further in studying rock damage. However, understanding the mechanical and fracturing properties of rocks is a complex problem, and the use of AE patterns to identify and predict rock ruptures entails various difficulties, such as selecting a suitable frequency band (FB) for monitoring rock failure predictions.

The present study conducts physical experiments on dry and saturated conditions using an AE-monitoring system to study the inner mechanism and unstable warning of rock fracturing, including the generation, development, and termination stages. Finally, for these research results, the AE signals must be identified, and the most suitable FBs for monitoring rock deformation and fracturing should be captured. This research will be important for predicting the final rupture of rocks.

## Basic theory of AE analysis in rock fracturing

AE waveform information of rock fracturing

AE refers to the generation of transient elastic waves produced by a sudden redistribution of stress and can result from the initiation and growth of cracks, slips, and dislocation movements in rocks. Therefore, the AE signal waveform is determined by the type of fracture source and affected by the propagation path and sensor performance.

The AE signals caused by rock fracturing differed widely due to the varied fracture origins, but they have two main types (He et al. 2010; Zhang et al. 2015). One is a burst form, which often appears early during rock failure; its waveform possesses a short increase time and rapidly reaches its peak before slowly decreasing (Fig. 1a). The other is continuous form, which generally appears when multiple fractures occur simultaneously (Fig. 1b), resulting in the difficult localization of the fracture/AE origins. This problem may be resolved by further developing the AE-monitoring equipment or AE machine parameter settings.

Thus, the typical AE signal of rock fracturing can be divided into burst and continuous signals.

Fig. 1 Typical AE signal of rock fracturing (Chen 1977; He et al. 2010; Zhang et al. 2015)

a Burst signal

b Continuous signal
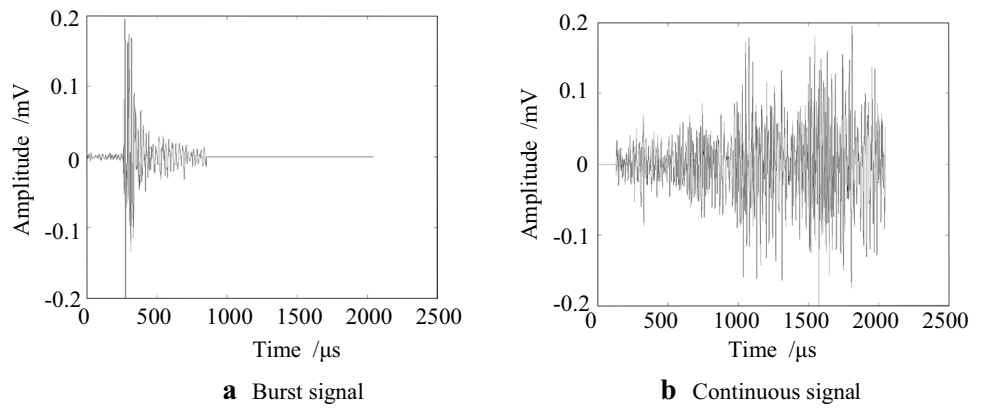
Fig. 2 AE waveforms in the time and frequency domains

a Time domain
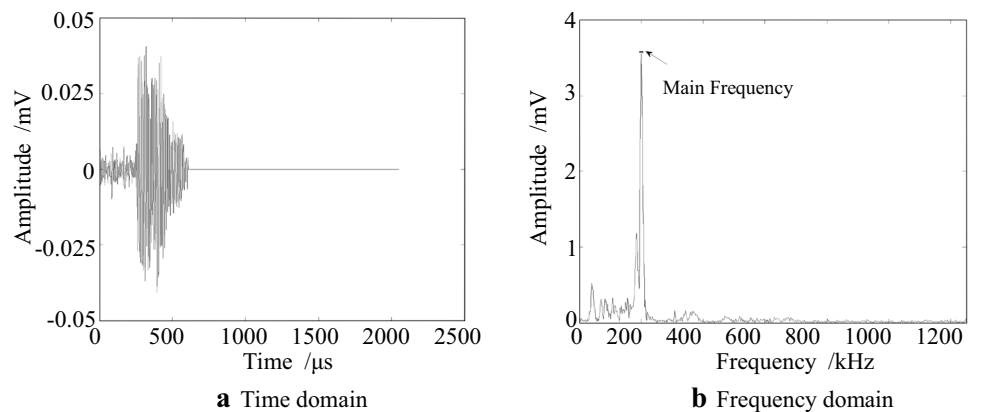
b Frequency domain

Figure 2 shows a typical AE signal (Fig. 2a) and its frequency distribution (Fig. 2b). The frequency characteristics are obtained using the fast Fourier transform. The signal is determined through spectral frequency analysis, and the main frequency is the highest frequency amplitude.

Value of rise time/amplitude (RA) and average frequency (AF)

The RA value is the rise time divided by the amplitude. The AF (unit: kHz) is defined as the ratio of threshold crossings divided by the signal duration. The RA and AF can be used to analyze the fracture types, which are presented in Eqs. (1) and (2), respectively (Ohtsu et al. 2007; Shiotani 2008):

$$RA = \frac{Rise\ Time}{Amplitude} \tag{1}$$

$$AF = \frac{Counts}{Duration\ Time}. \tag{2}$$

The cracking type can be classified by the following factors (Farhidzadeh et al. 2014): (1) Mode I, tensile crack, with high AF and low RA values and (2) Mode II, shear movement, with low AF and high RA values (Fig. 3).
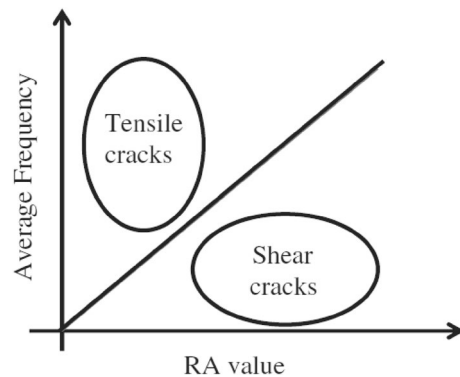
Fig. 3 Conventional crack classification (Farhidzadeh et al. 2014)

Fundamental principle of wavelet packet decomposition (WPD)

Wavelet packet transform is a useful tool for signal processing. Wavelets are oscillations resulting from multiple small wavelets and are often analyzed using polynomial, sine, cosine, and other functions (Mallat 1989; Cleophas and Zwinderman 2013). Various actual and simulated transient signals have been analyzed using the discrete wavelet transform, which demonstrates the power of wavelet analysis.

Wavelet packet analysis can decompose the high and low frequencies of an original AE signal. Decomposition must not occur in numerous layers; otherwise, the calculation redundancy is increased, which affects the processing speed, although few layers will not provide useful FB selection (Torresani 1992).

The WPD has the characteristics of orthogonality, independence, and multi-resolution, and its layer number is determined by the signal and requirements for feature parameters. After decomposition, the frequency range of each FB can be solved by the following formula:

$$f(j, i) = \left[\frac{f_s(j-1)}{2^{(i+1)}}, \frac{f_s j}{2^{(i+1)}} \right], \tag{3}$$

where $f(j, i)$ is the frequency range of the number j of FB after i layer decomposition ($j = 1, 2, \ldots, 2^i$) and f_s denotes the sampling frequency.

In the multi-resolution analysis, $L^2(R) = \oplus W_j\ (j \in \mathbf{Z})$, indicating that the analysis decomposed the $L^2(R)$ of Hilbert space into $W_j\ (j \in \mathbf{Z})$ of the orthogonal collections in accordance with different scale factors. WPD is expressed as follows:

$$W_j = \bigoplus_{m=0}^{2^k - 1} U_{j-k}^{2^k+m} \quad j, k, m \in \mathbf{Z} \tag{4}$$

$j = 1, 2, \ldots; k = 1, 2, \ldots, j; m = 0, 1, 2, \ldots, 2^k - 1$, where k is the number of decompositions and m represents the position number of decomposition FB.

We used $x(i)$ of the discrete signal to WPD, and x_{2^k+m} of the decomposed signal belongs to $U_{j-k}^{2^k+m}$ of the sub-space. N indicates the length of $x^{k,m}(i)$ of the discrete signal, and the energy can be expressed as

$$E_n(x^{k,m}(i)) = \frac{1}{N-1} \sum_{i=1}^{N} (x^{k,m}(i))^2. \tag{5}$$

The energy of every sub-FB can be represented by the percentage of total energy using the method of normalized relative energy. The relative energy of m-band can be solved as follows (Yen and Lin 2000):

$$E_n(m) = \frac{E_n(x^{k,m}(i))}{E_n(x(i))}. \tag{6}$$

Characteristics of AE signals during rock fracturing

Characteristics of AE signals

Rock material is typically non-continuous with the characteristics of non-uniformity and anisotropy, and its initial rupture has certain randomness. The appearance of rupture area

localization is important to final failure due to the evolution of fracturing process. Therefore, the AE generated by rock fracturing should have the following characteristics:

- Rock fracturing occurs rapidly but produces large amounts of AE signal data. The wavelet basis function should be selected to handle large data.
- Various rocks have different geological settings, and a given rock will have multiple scales of flaws, which will influence its AE signal. The wavelet basis function should be sensitive to flaw signals and insensitive to external disturbances.
- The particulate nature of a rock leads to the distribution of numerous micro-structure planes inside it, which can produce AE signals with different frequencies under various stress levels and modes. The wavelet basis function should be selected to provide compact support and attenuation, given that AE signals are abrupt and complex.

Discrete wavelet packets offer more compact calculations and faster processing than continuous wavelet packets, thereby rendering them favorable for processing the large data sets associated with AE signals.

Introduction of wavelet packet transform during AE signal processing

In "2.3 The fundamental principle of wavelet packet decomposition (WPD)," CA*i* and CD*i* (the low- and high-frequency components of AE signals, respectively) are decomposed to create the full binary tree. For *n* levels of decomposition, the WPD produces 2^n different sets of coefficients (or nodes).

Experimental investigations

Rock samples and preparation

Gabbro is a large group of dark, often phaneritic or coarse-grained, mafic intrusive igneous rocks that are chemically equivalent to basalt. Gabbro forms when molten magma is trapped beneath the Earth's surface and slowly cools into a holocrystalline mass. Most of the oceanic crust is composed of gabbro, which is formed at mid-ocean ridges. Gabbro is also found as plutons associated with continental volcanism.

All samples were processed into cuboids of 50 mm × 50 mm × 100 mm. Dry and saturated samples were prepared as follows. (1) Dry samples: five rock samples were oven-dried at 105 °C for 48 h. (2) Saturated samples: five rock samples were prepared through the free water absorption method. The samples were partially immersed for 2 h in a water sink, in which one quarter of each is covered.

The water depth was then increased to half coverage for an additional 2 h. Three-quarters of the samples were immersed for another 2 h and then finally fully submerged for 48 h before use.

Table 1 lists the experimental and loading conditions of all 10 samples of gabbro specimens.

Experimental setup and method

The experimental system comprises the loading and AE systems (Fig. 4).

- *Loading system* Compression tests were conducted on a servo-controlled rock-testing machine (ATW-3000, Chaoyang Test Instrument Corporation, Changchun, China). The deformation and applied vertical force can be monitored. The capacity of the axial load transducer is up to 3000 kN.
- *AE-monitoring system* The AE activities of rock fracturing were recorded using an AE detector with eight channels. The multi-parameter AE data, including waveform, hit, ring-down counts, and amplitudes, are obtained using a computer-based AE system (PCI-2, Physical Acoustic Corporation, NJ, USA).
- *AE Sensor* The AE sensor selected was a resonance type, namely, PAC Type R6α, with a resonance frequency of 45 kHz. The response FB of R6α ranges from 0 to 120 kHz. The AE sensor is a typical ceramic piezoelectric element.

The equipment setup should be consistent to guarantee the conformity of the experimental data (Ishida et al. 2017). The sampling time was set at 0.2 μs, and a memory length was set at 2 k (2048 words). In this case, the recording time period was approximately 0.4 ms (0.2 μs × 2048). The pre-trigger was set at 1 k, and the sampling rate was set at 1 MHz.

With regard to noise handling, this experimental environment has two main noise sources. The first type of noise, which is caused by the end effect, is minimized by controlling the non-parallelism of the two ends to less than 0.02 mm. The second type of noise, i.e., touching noise, can be produced when rock samples are in contact with the terminal of the loading system. A 10 kN preload was applied to reduce the touching noise. In addition, a high-strength adhesive was used to ensure a good connection between the caps and samples.

Testing results

Analysis of rock mineral composition

The experiment of mineral species identification (Fig. 5) established the content of each mineralogical component, including augite (25–30%), carbonate (20–25%), magnetite (35–40%), quartz, and calcite. Weathering action induced severe clay alteration in the rocks' carbonate components.

Weathering action can decompose "III carbonate" components into calcite minerals, which in turn can react with water in saturated samples. Calcite dissolution can destroy the micro-structural integrity in the saturated gabbro specimens, rendering them prone to cracking.

### Analysis of rock failure evolution

Figure 6 shows the curves for stress, AE energy, and AE-accumulated energy with respect to the loading time of the two types of rock specimens. The AE energy and AE-accumulated energy during the entire loading process can be divided into four stages.

Stage I, the initial stage (OA) The rock has slight deformation and low deformation rate with weak AE activity. The AE energy and AE-accumulated energy are distributed at a low level, resulting from opening or closing micro-cracks in the specimens.

Table 1 Dimension of rock samples and loading conditions

Water conditions	No.	Control model	Loading rate (N/s)	Dimension (mm³)
Dry	GXW-1	Force	500	50.02 × 49.86 × 100.04
	GXW-2			50.12 × 49.54 × 99.98
	GXW-3			51.06 × 50.62 × 100.32
	GXW-4			49.92 × 50.86 × 99.60
	GXW-5			50.42 × 49.92 × 100.14
Saturated	HSXW-1	Force	500	50.34 × 49.96 × 99.64
	HSXW-2			50.22 × 50.52 × 100.38
	HSXW-3			50.14 × 50.82 × 100.52
	HSXW-4			50.32 × 51.02 × 100.02
	HSXW-5			50.80 × 48.98 × 100.10

Fig. 4 Experiment equipment. **a** Experiment system; **b** loading system; **c** AE-monitoring system; **d** acquisition card; **e** preamplifier
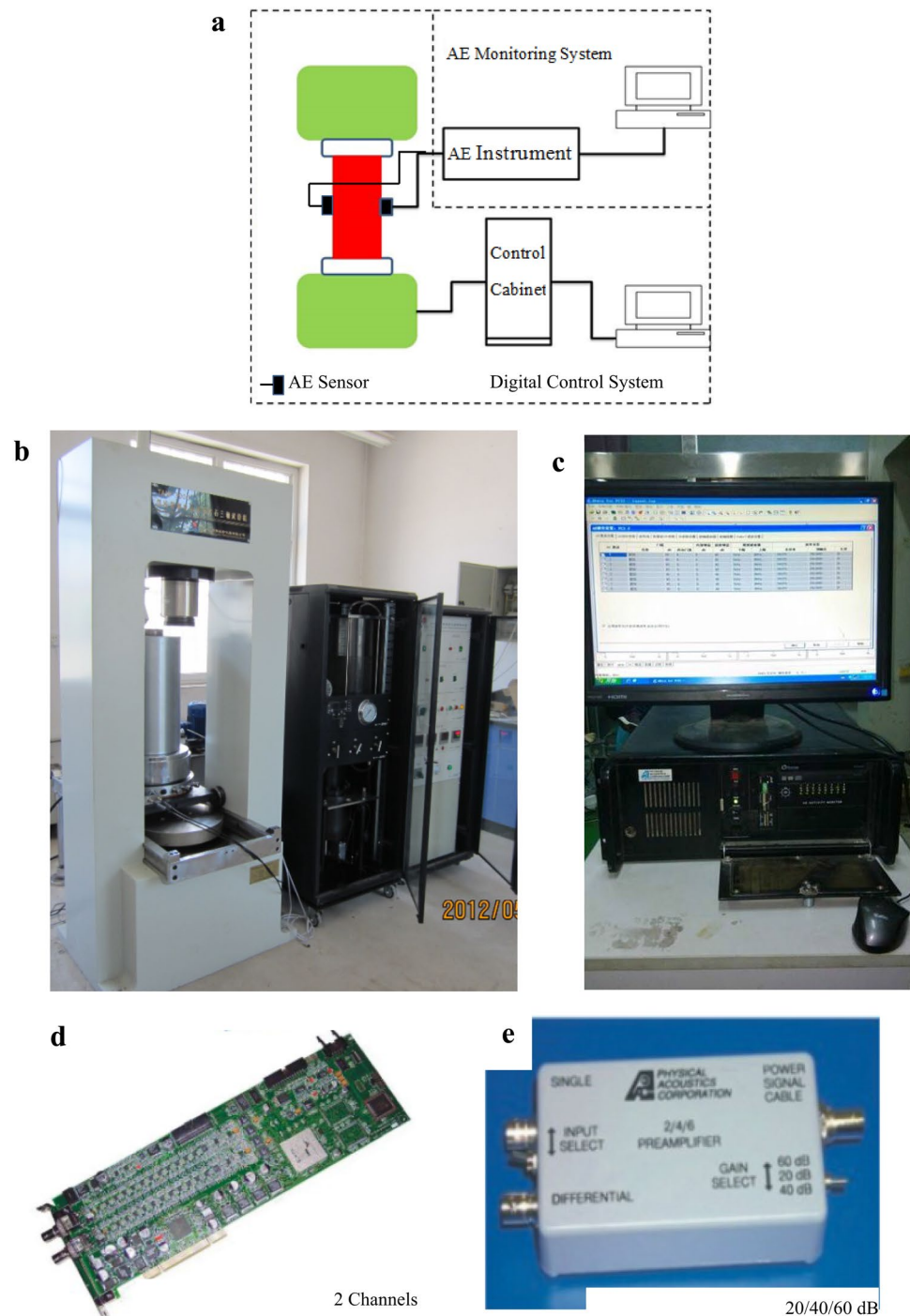
Stage II, the linear elastic stage (AB) The rock specimens cannot be damaged, and the AE activity has almost stopped.

Stage III, the nonlinear elastic stage (BC) When the rock mass is near the final fracturing, the deformation rate will increase, and the rock mass is gradually transformed from the steady state to the unstable state. The stress curve remains linear; however, the AE energy and AE-accumulated energy curves show that rupture has occurred, but did

not affect the bearing capacity of the rock. The AE-accumulated energy curves in this stage indicate distinctive breaking characteristics similar to a number of shear-damaged "rock bridges."

Stage IV, the final breaking stage (CD) The rock mass is unstable at the rock fracturing stage, and the deformation rate increases rapidly. Several peak numbers of stress appear, and the AE-accumulated energy reaches its peak.

The stress, AE-accumulated energy, and AE energy curves undergo several oscillations during this period.

Rock fracture analysis

**Macroscopic crack analysis** All 10 gabbro samples were tested at this uniaxial experiment. Figure 7 shows the typical fracture patterns of the dry and saturated samples. Figure 7a presents a typical fracture of a dry sample that appears as a double cone body; tensile (C1) and shear (S1) fracturing surfaces are observed in rocks. Figure 7b displays a typical fracture of a saturated sample that appears as a single cone body; several parallel cracks, which passed through the whole specimen from bottom to top, accompanied by

Fig. 5 Chemical composition distribution/10×10(+). I—Augite; II—plagioclase; III—carbonate; IV: aggregate of carbonate; V—magnetite

a Sample 1#   **b** Sample 2#

a Dry samples   **b** Saturated samples
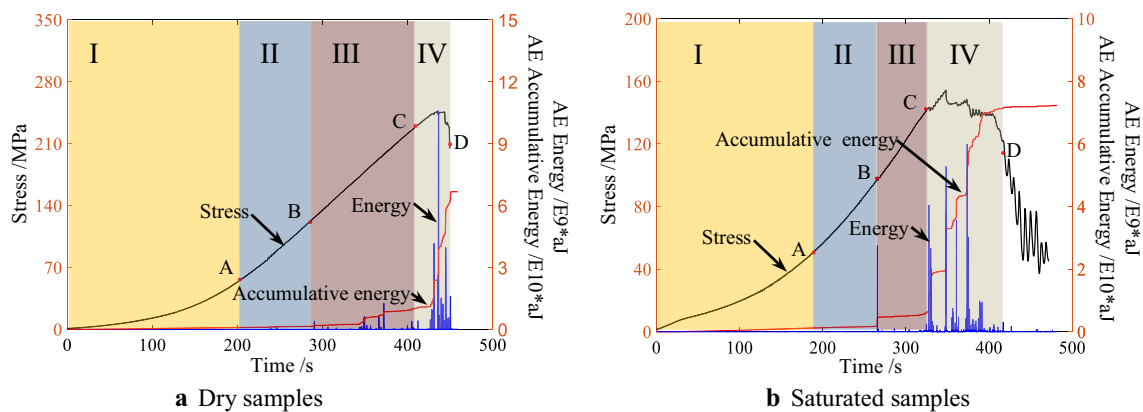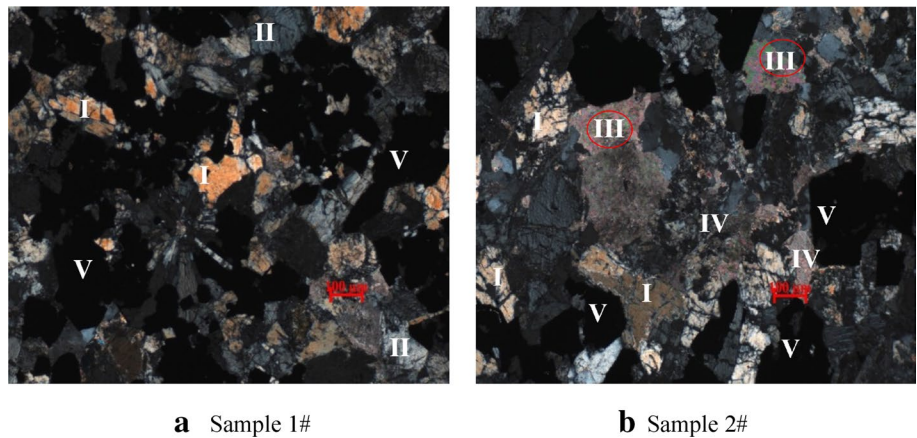
Fig. 6 Stress, energy, and accumulative energy curves of AE versus the loading time of rock specimens

Fig. 7 Fracture patterns of the dry and saturated specimens

a Dry sample   **b** Saturated sample
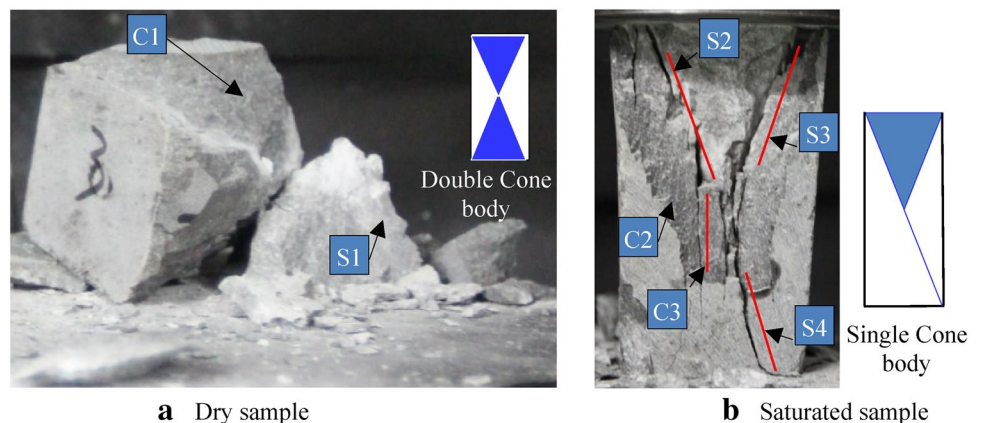
small cracks, are observed. Shear (S2, S3, and S4) cracks are labeled. Crack patterns of numbers C2 and C3 exhibit a tensile fracturing mode. In addition, a small scale of tensile cracks can be seen in the saturated specimen.

Dry and saturated specimens show the same fracturing modes. A common cracking pattern involves shear and tensile cracks. The observed rupture is caused by a typical shear–tensile failure. Both specimens had the same distribution of mineral particle sizes and hardness of mineral grains despite varying micro-geological structures. However, the carbonate ingredients of saturated samples undergo severe clay alteration. The differences in the rupture intensity show that dry samples are more brittle than saturated samples.

Mesoscopic crack analysis RA and AF presented a statistical relation (Appendix 3), and the influence of water on the cracking model is shown in the results of this study. During the test, four typical periods (Fig. 8), namely, stage I (the initial stage, OA), stage II (the linear elastic stage, AB), stage III (the nonlinear elastic stage, BC), and stage IV (the final breaking stage, CD), were divided in the rock deformation and fracture processes in accordance with the AE parameter distribution of RA versus AF. Figure 8 shows the corresponding density maps of crack distribution during rock fracturing evolution in the dry and saturated samples. The distribution densities in blue color are lower than those in red color (color bar in Fig. 7). Thus, the tensile crack is more intensive than the shearing crack in the rock fracturing process between dry and saturated samples. These two watery states have common characteristics, and the percentage of shearing crack presents a remarkable positive correlation in the first three stages (the initial, linear elastic, and nonlinear elastic stages) and negative correlation in the last stage (the final breaking stage).

A comparison shows that the AF value of the dry sample is higher and its tension fracturing is more developed than those of the saturated sample. However, the RA value of the saturated sample is greater, indicating that the shearing failure of saturated rock is higher than that of the dry sample. Tension and shearing are fracture types with low- and high-energy releases, respectively; these characteristics can be observed in the AE energy curves (Fig. 6).

The severe carbonate-to-clay transformation at watery state is accompanied by calcite formation. Unlike in dry samples, the saturated granules chemically react, thereby destroying their structural integrity and leading to tensile cracking that easily occurs in the saturated gabbro samples. In general, water conditions can change the crack distribution of rock fracturing evolution. Susceptibility to shear cracking happened in saturated rock during the uniaxial loading process due to water non-shearing characteristics.

Figures 6, 7 and 8 indicate the formation of a number of shear-damaged surfaces on the rock samples. The mechanics

and AE characteristics show that water reduces the intensity of rock failure. The dry samples suffer complete collapse, whereas the saturated samples remain whole. The uniaxial compressive strengths of dry and saturated samples are 246.7 and 154.5 MPa, respectively. Both the types of samples undergo multiple bursts of "rock bridge" modes. The AE-accumulated energy is expressed as a ladder, and the AE energy is set as a peak number with an intermittent appearance.

A unified law of rock deformation and fracturing is difficult to achieve due to the complexity and fracturing conditions of the rock, which renders the rock displacement monitoring method difficult to use for determining rock stability. Furthermore, the plastic deformation appears before the complete destruction of the saturated samples.

AE frequency features during rock fracturing evolution

AE frequency division processing

The selection of an optimal wavelet basis is important for analyzing and processing AE signals. The primary function of the Daubechies wavelet series is compact, smooth, and nearly symmetric with different sequences (dbN) for various positive integers. Given the aforementioned characteristics of AE signals, the db6 wavelet basis function is suitable for processing rocks' AE signals.

The AE-monitoring system had a sampling rate of 1 MHz. On the basis of the Nyquist sampling theorem (Nyquist 2002), the Nyquist frequency was set to 500 kHz, leading to a decomposed FB in the range of 0–500 kHz. Four decomposed layers were selected in this study. The distribution of each FB layer is decomposed by wavelet packets (Appendix 1).

The energy amount ratio (energy spectrum coefficient), as a characteristic parameter of AE signals, provides an effective evidence for determining rock failure. Table 2 in Appendix 2 shows the energy ratio of each layer decomposed by wavelet packets. Figure 9 depicts the energy amount ratios of each layer.

Figure 9a presents the tree of four WPD layers. Figure 9b, c shows the AE signal energies for dry and saturated states, respectively, mainly focusing on CA41, CD42, CA43, and CD44; the corresponding FBs are in the range of 0–125 kHz.

Monitoring FB during rock fracturing

Definition of precursor advantage FB

The formation of rock cracks, including the initiation, propagation, and coalescence of micro-cracks, has statistical
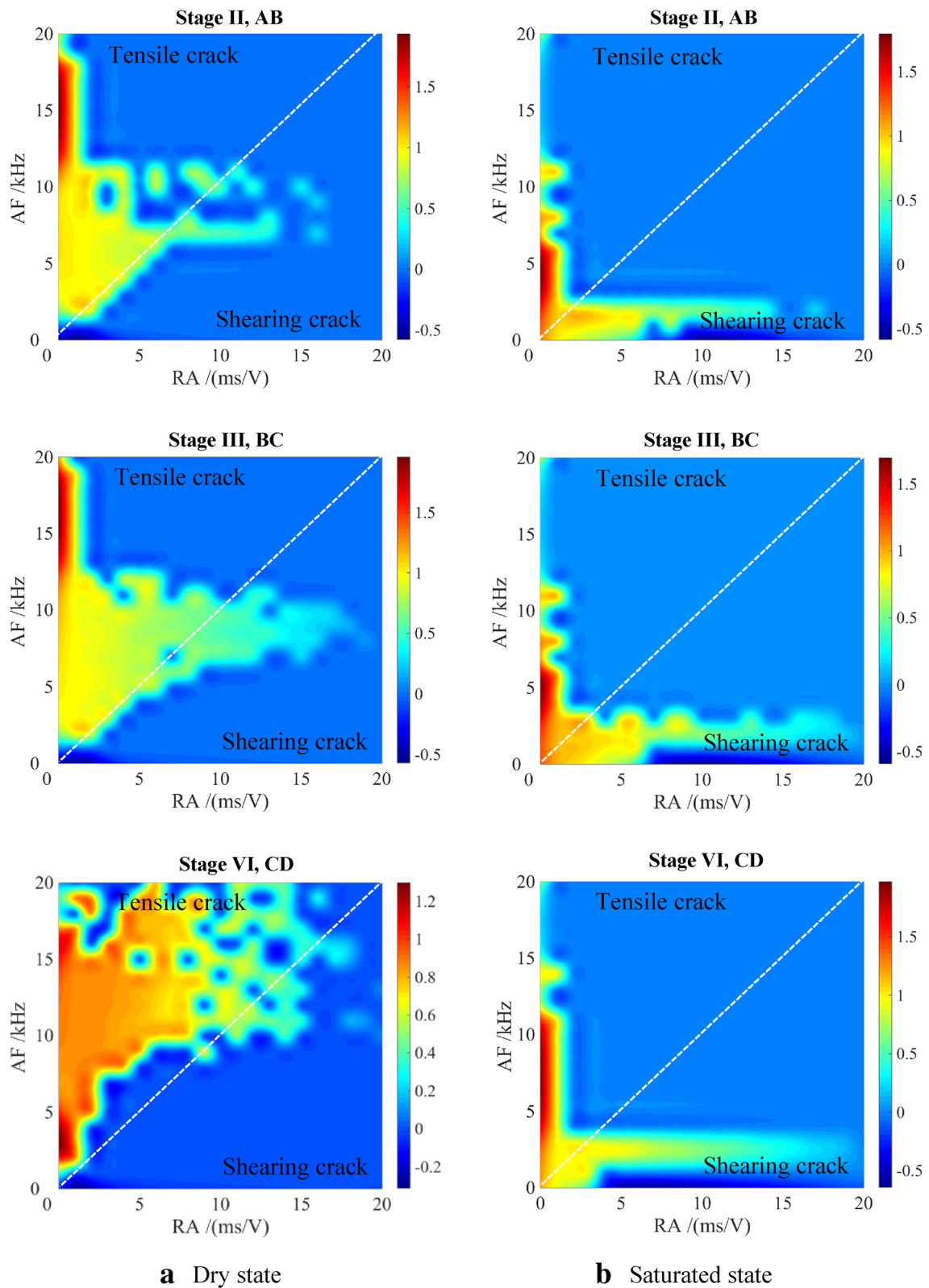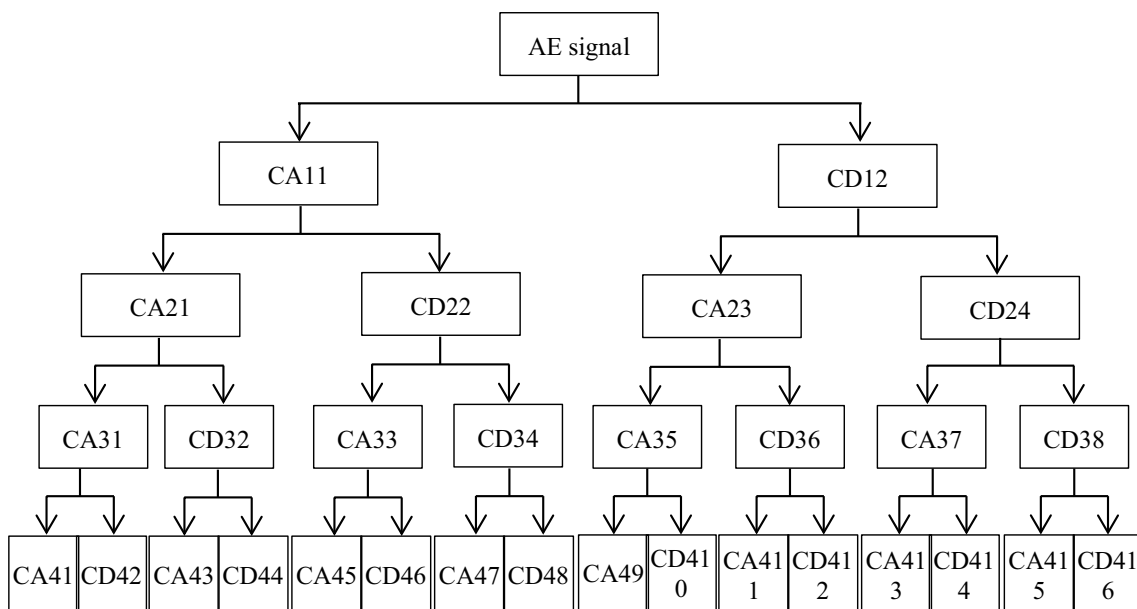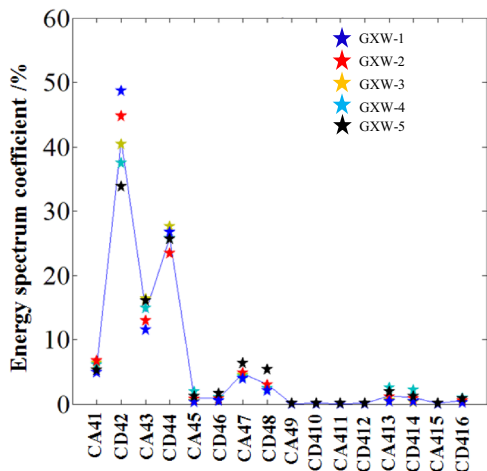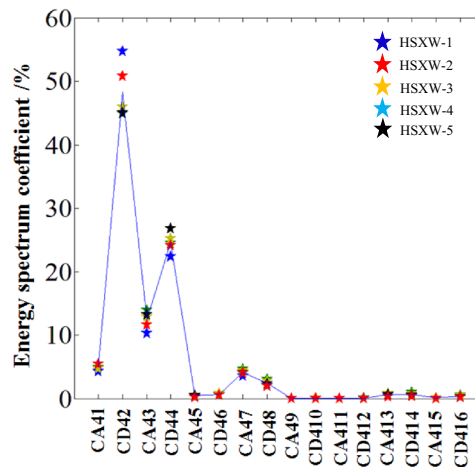
a Dry state   **b** Saturated state

Fig. 8 Crack model of dry and saturated states

a WPD tree

b Dry state

c Saturated state

Fig. 9 Energy amount ratio of each layer under dry and saturated states

fractal features (Bahat et al. 2001; Ma et al. 2011; Li et al. 2015). AE and micro-cracks can be caused by element failure, thereby gradually damaging the rock (Liang et al. 2007). The frequency distribution of AE can vary from a state of disorganization or incoherence to a concentrated response and is associated with the conditions of moisture, rock type, fracture morphology, and stress state. Certain correspondence is observed between frequency and fracture patterns (Enomoto and Hashimoto 1990; He et al. 2015).

A precursor advantage FB is relatively sensitive to buckling failure in the AE frequency domain corresponding to rupture. The establishment of FB is a reliable reference for predicting rock instability and failure.

Algorithm for FB monitoring

The selected precursor advantage FB is used as a reference signal and detected as the first AE signal received from the rock fracture. A value for characteristic parameter C can be selected. h is the changed value at time t. $\Theta_i(t)$ indicates the sample observation of the rock fracture at time t. $r_i(t + \Delta t)$ represents a fundamental function from time t to time $(t + \Delta t)$ and can be solved as follows:

$$r_i(t + \Delta t) = \Theta_i(t + \Delta t) - C_i, \tag{7}$$

$r(t)$ can be decomposed using wavelet packets:

$$
\left.\begin{array}{l}
r_{CA1}(t + \Delta) = \Theta_{CA1}(t) - C_{CA1} \\
r_{CD2}(t + \Delta) = \Theta_{CD2}(t) - C_{CD2} \\
\quad\quad \dots\dots \\
r_{CAi}(t + \Delta) = \Theta_{CAi}(t) - C_{CAi} \\
r_{CDi}(t + \Delta) = \Theta_{CDi}(t) - C_{CDi}
\end{array}\right\}.
$$

The variable energy coefficient (VEC) ζ can be defined as follows:

$$
\zeta_i = \frac{r_i(0, h)}{C_1} = \frac{\Theta_i(t) - C_1}{C_1}. \tag{8}
$$

The wavelet decomposition with i levels for ζ is as follows:

$$
\left.\begin{array}{l}
\zeta_{CA1} = \frac{r(0,h)}{C} = \frac{\Theta_{CA1}(t) - C_{CA1}}{C_{CA1}} \\
\zeta_{CD2} = \frac{r(0,h)}{C} = \frac{\Theta_{CD2}(t) - C_{CD1}}{C_{CD2}} \\
\quad\quad \dots\dots \\
\zeta_{CAi} = \frac{r(0,h)}{C} = \frac{\Theta_{CAi}(t) - C_{CA1}}{C_{CA1}} \\
\zeta_{CDi} = \frac{r(0,h)}{C} = \frac{\Theta_{CDi}(t) - C_{CD1}}{C_{CD1}}
\end{array}\right\}.
$$

The precursor advantage FB is the most remarkable during unstable rock fracture, and its VEC is expressed as $\zeta_i = \zeta_{max}$.

### Relation analysis of VEC with respect to time

The analysis of a specific parameter of the selected sub-signal of the wavelet packet (CA41–CD416) considers the reference signal as the C value. $\Theta(t)$ is the numerical value of the wavelet energy spectrum of each AE signal during rock rupture. Previous research has confirmed that the layers from CA41 to CD44 are the FBs with the greatest energy in the AE signals.

Figures 10 and 11 show the relationship between ζ (CA41, CD42, CA43, and CD44) and t, indicating that watery state affects the deformation and fracturing of gabbro rock. ζ_{CA41} rapidly increased in the dry and saturated states near the final buckling failure, which is a catastrophic model for the rock instability failure.

By comparing ζ_{CA41} in dry and saturated samples, the amplitude of saturated samples is considerably greater than other ζ, and the amplitude of dry samples varies. This
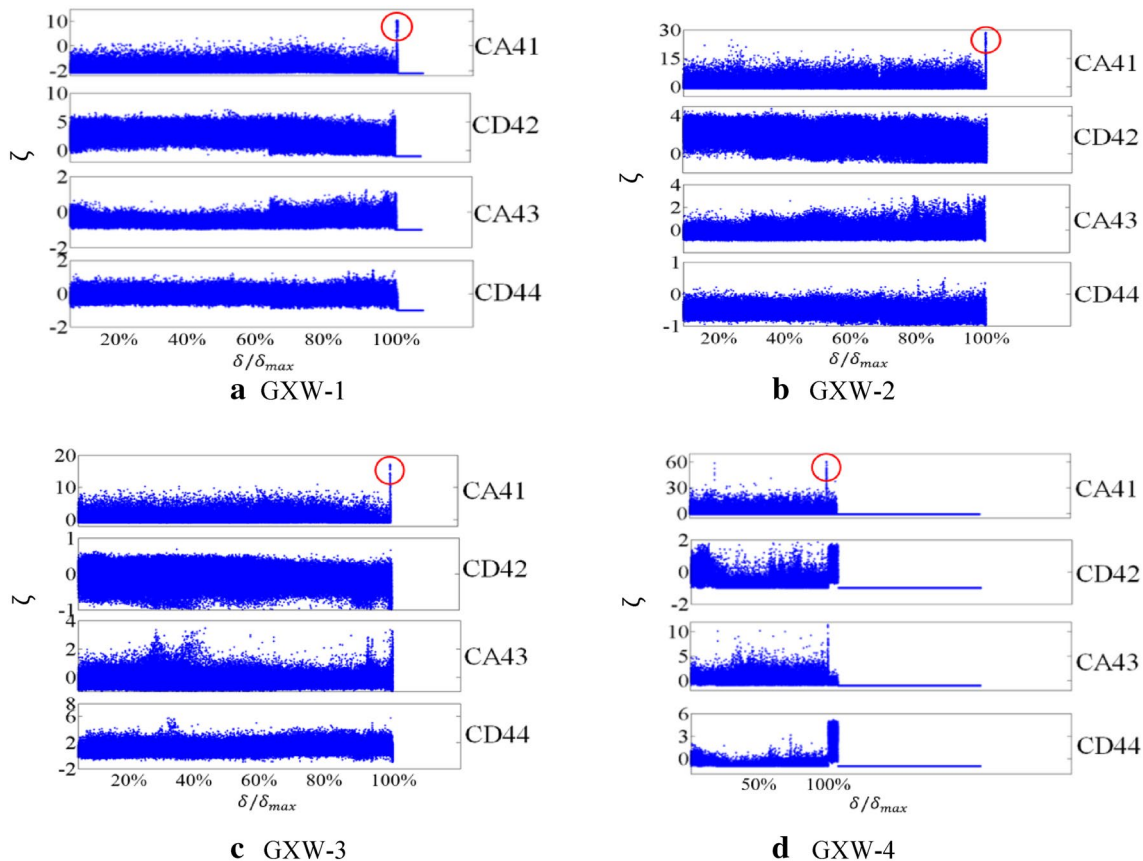
Fig. 10 Waveletpacket of $\zeta - t$ from layer CA41 to CD44 for the gabbro samples under dry state
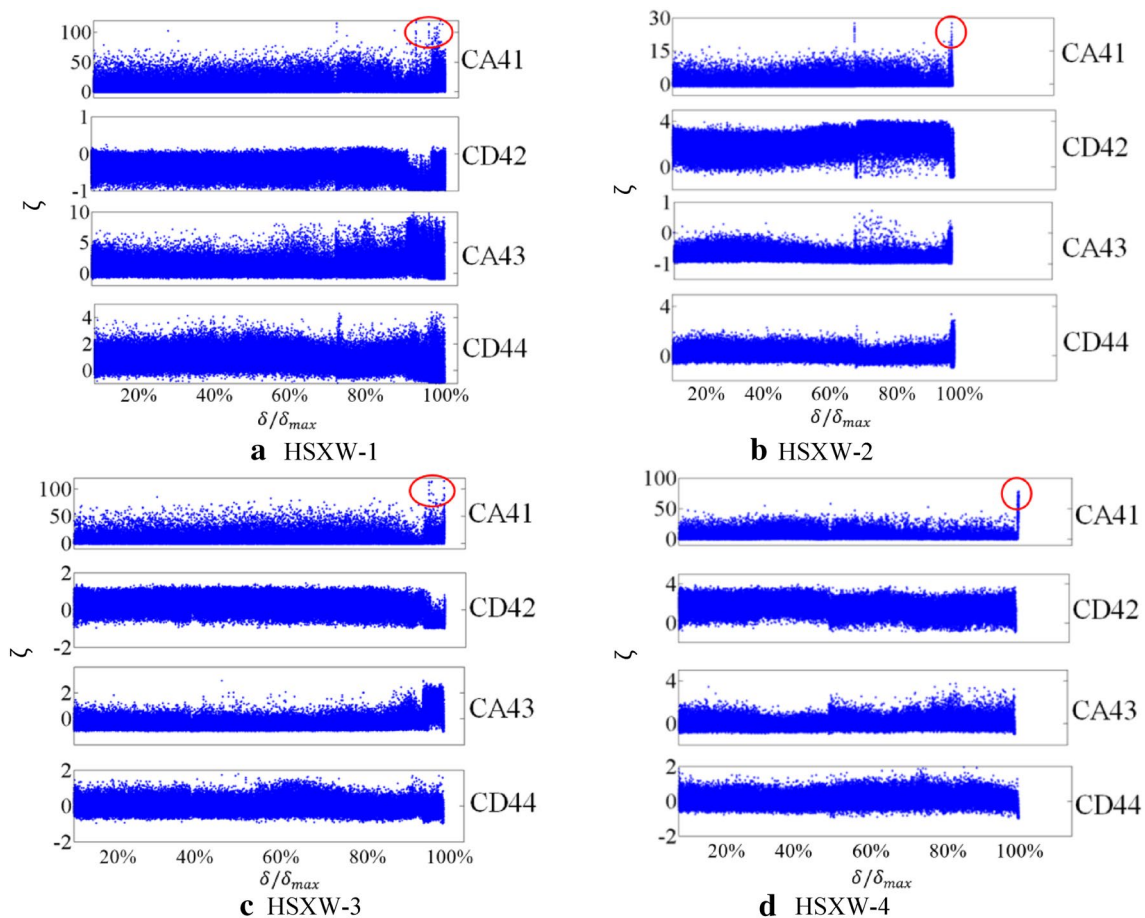
Fig. 11 Waveletpacket of $\zeta - t$ from layer CA41 to CD44 for the gabbro samples under saturated state

phenomenon reflects how the fracturing evolution of saturated rock is more unified than that of dry rock.

Moreover, ζ_{CA41} present similar signals that can be found in the early stage, e.g., a remarkable increase of ζ_{CA41} can also be found in 20% (Fig. 10d), 75% (Fig. 11a), and 70% (Fig. 11b). These results reflect the complexity, fracturing conditions, and original defect distribution of the rock; ζ is closely related to the rock fracturing activity. The rock maintains integrity in the first four stages, the transmission of AE signal remains complete, and the speeding rate of AE signal is fast. The signals easily overlap one another, and this similar situation occurs.

Applying the VEC alone to the instability forewarning of the rock is insignificant. In "3.3.2 Analysis of rock failure evolution," the entire loading process can be divided into four stages: stage I (the initial stage, OA), stage II (the linear elastic stage, AB), stage III (the nonlinear elastic stage, BC), and stage IV (the final breaking stage, CD). Unstable fracturing of the rock is predicted to only happen in the final breaking stage (stage IV, CD).

Therefore, the stress condition should also be combined to analyze the short-term forecasting work using the VEC.
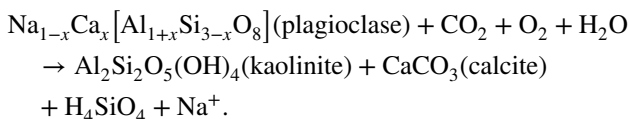
Discussion

Action mechanism of free water on rock fracturing

The influence of water on the properties of rock material and its fracturing evolution can be analyzed from the aspects of chemical function ([1] weathering and [2] hydration actions) and physical function ([3] immersion wetting).

1. "Weathering action" of rock exposed to the air

The weathering action is complicated, with two chief considerations, namely, oxidizing and hydrolytic reactions. The typical chemical reactions performed can be shown as follows:

$$Na_{1-x}Ca_x\left[Al_{1+x}Si_{3-x}O_8\right](\text{plagioclase}) + CO_2 + O_2 + H_2O$$
$$\rightarrow Al_2Si_2O_5(OH)_4(\text{kaolinite}) + CaCO_3(\text{calcite})$$
$$+ H_4SiO_4 + Na^+.$$

2. "Hydrating action" of the bubble water process

After the weathering action, the plagioclase constituent is converted into the "III carbonate" constituent (e.g., kaolinite and calcite). The water soluble or hydrating reaction is easy to find in this constituent. The typical chemical reactions performed can be shown as follows:

$$CaCO_3(\text{calcite}) + CO_2 + H_2O \leftrightharpoons 2HCO_3^- + Ca^{2+}.$$
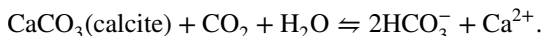
Furthermore, some kaolinite constituent can be formed in the weathering action. The kaolinite constituent has high water absorption. The montmorillonite, illite, or halloysite can be formed on the basis of the amount (x) of bound water:

$$Al_2Si_2O_5(OH)_4(\text{kaolinite}) + H_2O \rightarrow Al_2Si_2O_5(OH)_4 \cdot xH_2O$$
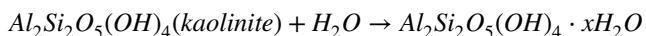
3. "Immersion wetting" of rock fracturing experiment

Immersion wetting has marked down the friction force of shearing slip; the saturated sample easily forms the slipping cracks.

Thus, on the basis of the aforementioned actions (chemical and physical functions), the water destroyed the cohesion of mineral particles in the saturated rock. The low energy and intermediate frequency of AE signals will appear with the fracturing evolution.

Most suitable FB to distinguish the dry and saturated states of rock

Contrast analysis of AE signal in FB features

The experimental study of the AE associated with inelastic processes, such as tensile and shear cracking, during the deformation of rocks offers an excellent method for investigating the mechanism of brittle fracture (Gowd 1980). These cracking modes during the deformation of brittle rocks offer different FBs in the AE signals. Therefore, the analysis of FBs in the AE can distinguish the fracture model and thus whether a gabbro sample is in a dry or saturated state:

$$\Delta E_i = E_i(\text{saturated}) - E_i(\text{dry}), \qquad (9)$$

where $i = CA41 \sim CD416$, $E_i(\text{saturated})$ is the energy coefficient of the sub-signal after WPD while fracturing the saturated samples, and $E_i(\text{dry})$ denotes the energy coefficient of the sub-signal after WPD while fracturing the dry samples.

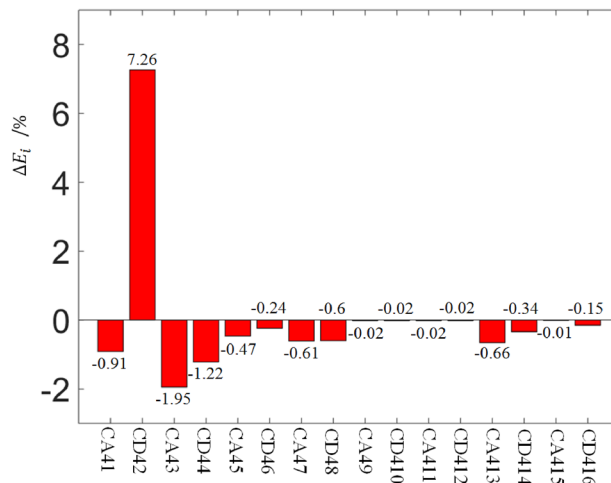In Fig. 12, the FBs at 0–31.25 (layer CA41), 62.5–93.75 (layer CA43), and 93.75–125 kHz (layer CD44) show that

Fig. 12 Column diagram of each layer ratio of energy amount under dry and saturated states

water saturation reduced the energy concentration coefficient. However, water saturation increased the energy concentration coefficient in the FBs of 31.25–62.5 (layer CD42) and 31.25–62.5 kHz (layer CD42), which was also the most sensitive to the effect of water. Table 3 in Appendix 3 presents the data on the energy concentration of the sub-FB between the dry and saturated states. Figure 12 shows that the saturated state showed greater frequency spectrum coefficients than the dry state, except for the FB of 31.25–62.5 kHz (layer CD42: $\Delta E = +7.26$, the highest magnitude ΔE value). This FB was the largest and most sensitive to water and thus is promising for investigating and comparing the moisture state of rocks during deformation and fracturing. The FB of 62.5–93.75 kHz (layer CA43) showed the smallest ΔE number of -1.95.

Overall, the moisture condition altered the microscopic grains of gabbro, which is beneficial to the tensile cracking of the soaked samples. The 31.25–62.5 kHz FB of the gabbro is attributed to tensile cracking.

Precursor advantage of FB selections

Relationship between the AE frequency domain and physical form of cracks

The characteristics of AE frequency value and the physical form of cracks are correlated (Haskell 1964; Ohnaka 1976):

$$f \sim \frac{1}{[T + (c/v)(1 - (v/\beta)\cos\theta]}, \qquad (10)$$

where T refers to the time of closings, openings, or slips of cracks. c denotes the length of cracks. v represents the

velocity of produced cracks. θ indicates the angle between the crack surface and propagation direction of AE signals. $\sim$ is the symbol for correlation.

Formula (10) shows that the parameters of T and c have a negative correlation to frequency value. This result indicates that the AE signal has a low-frequency distribution when the fracture scale increases and coasts at fracturing formation for a short time. The evolution of rock damage is the development of the fracture size from the micro-scale to macro-scale. Thus, the sudden increase in response to low FBs is an inevitable phenomenon along with the fracturing evolution.

Selection of precursor advantage FB

The analysis in Section "Monitoring FB during rock fracturing" indicated that several FBs in each moisture state experience rapid and large changes, but 0–31.25 kHz (layer CA41) can be selected as the precursor advantage FB for three main reasons.

First, during the final rupture process, the micro-fractures gradually accumulated and expanded, and the high-frequency component of the AE signal rapidly dampened during this transmission. The amplitude of the high-frequency component weakened to a large degree, but the low-frequency component weakened slowly.

Second, Formula (10) shows that the fractures increased in the middle and later fracturing periods. The FB area of the AE signal and the fracturing size presented a negative relationship.

Third, as axial stress increased, free water created a negative pressure in pores and was allowed to flow into them, thereby producing low-frequency signals. This finding agrees with the research findings of Benson and Burlini (Benson et al. 2008; Burlini and Toro 2008).

Different samples in the same moisture conditions have various numbers of ζ_{CA41}, but all ζ_{CA41} in different samples have the same property of catastrophe due to the anisotropy of the rock samples. Therefore, in this study, ζ_{CA41} can be used to monitor the final unstable fracturing in accordance with the characterization of rock fracturing through AE technology.

Conclusions

This work intends to establish the effect of water saturation on rock and the features of its AE frequency domain and then presents a new interpretation of the latter. Furthermore, we find specific FBs to characterize the unstable fracturing of rock and discuss interesting features related to the changes in the rock during its failure.

1. Water affects the physical and mechanical properties of fracturing. Dry and saturated samples experience shear, thereby damaging "rock bridges". Weathering induces severe clay alterations, thereby affecting the carbonate components of gabbro rock.
2. The different FBs of the AE signal can describe the information about the rock's physical properties and mechanical processes, including the characteristics of damage evolution and fracture. The water induces distinctive fracture features. This research identifies the FB of 31.25–62.5 kHz as especially useful for distinguishing the saturation state of gabbro.
3. Under uniaxial loading, the precursor advantages of FB for gabbro rupture are in the range of 0–31.25 kHz during dry and saturated states in rock samples.

Appendix 1

See Table 2.

Table 2 Layered FB distribution of the wavelet packet

No.	CA41	CA43	CA45	CA47	CA49	CA411	CA413	CA415
Low-frequency band/ kHz	0, 31.25	62.5, 93.75	125, 156.25	187.5, 218.75	250, 281.25	312.5, 343.75	375, 406.25	437.5, 468.75
No	CD42	CD44	CD46	CD48	CD410	CD412	CD414	CD416
High-frequency band/ kHz	31.25, 62.5	93.75, 125	156.25, 187.5	218.75, 250	281.25, 312.5	343.75, 375	406.25, 437.5	468.75, 500

Appendix 2

See Table 3.

Table 3 Layer energy spectrum coefficients of gabbro decomposed by the wavelet packet in dry and saturated states

Moisture	Sample No.	Ratio of energy amount /%															
		CA 41	CD 42	CA 43	CD 44	CA 45	CD 46	CA 47	CD 48	CA 49	CD 410	CA 411	CD 412	CA 413	CD 414	CA 415	CD 416
Dry	GXW-1_1	6.39	40.43	16.27	27.61	0.43	0.47	4.48	2.47	0.05	0.06	0.06	0.05	0.59	0.34	0.07	0.22
	GXW-2_2	6.13	37.43	14.85	25.77	1.89	0.99	4.23	2.46	0.06	0.12	0.11	0.16	2.53	2.18	0.15	0.93
	GXW-3_1	6.71	44.75	12.91	23.46	0.72	0.85	4.82	2.94	0.08	0.10	0.09	0.08	1.07	0.83	0.11	0.48
	GXW-4_1	4.93	48.69	11.51	26.67	0.31	0.52	3.93	2.11	0.05	0.06	0.06	0.05	0.42	0.38	0.07	0.25
	GXW-5_1	5.29	33.86	16.03	25.61	1.22	1.67	6.34	5.34	0.14	0.15	0.13	0.13	1.91	1.23	0.16	0.80
	Average value	5.89	41.03	14.31	25.82	0.92	0.90	4.76	3.07	0.08	0.10	0.09	0.09	1.30	0.99	0.11	0.54
Saturated	HSXW-1_1	4.97	44.94	13.91	24.46	0.51	0.71	4.65	3.06	0.07	0.10	0.09	0.09	0.73	0.99	0.14	0.59
	HSXW-2_1	4.28	54.74	10.23	22.37	0.42	0.58	3.59	2.12	0.05	0.06	0.06	0.05	0.61	0.48	0.08	0.29
	HSXW-3_1	4.71	45.95	12.89	25.21	0.62	0.80	4.37	2.82	0.08	0.10	0.09	0.09	0.89	0.80	0.11	0.49
	HSXW-4_1	5.50	45.05	13.20	26.80	0.48	0.60	4.11	2.32	0.07	0.08	0.07	0.07	0.69	0.55	0.09	0.33
	HSXW-5_1	5.43	50.76	11.59	24.17	0.19	0.62	4.03	2.00	0.05	0.05	0.05	0.05	0.27	0.42	0.07	0.24
	Average value	4.98	48.29	12.36	24.60	0.45	0.66	4.15	2.47	0.06	0.08	0.07	0.07	0.64	0.65	0.10	0.39

Appendix 3

See Table 4.

Table 4 Energy amount ratio information of sub-FB under dry and saturated states

	Energy amount ratio information of sub-FB /%															
	CA 41	CD 42	CA 43	CD 44	CA 45	CD 46	CA 47	CD 48	CA 49	CD 410	CA 411	CD 412	CA 413	CD 414	CA 415	CD 416
E_i(saturated)	5.89	41.03	14.31	25.82	0.92	0.9	4.76	3.07	0.08	0.1	0.09	0.09	1.3	0.99	0.11	0.54
E_i(dry)	4.98	48.29	12.36	24.6	0.45	0.66	4.15	2.47	0.06	0.08	0.07	0.07	0.64	0.65	0.1	0.39
$\Delta E_i = E_i$(saturated) $-E_i$(dry)	-0.91	7.26	-1.95	-1.22	-0.47	-0.24	-0.61	-0.6	-0.02	-0.02	-0.02	-0.02	-0.66	-0.34	-0.01	-0.15

References

Armstrong BH (1969) Acoustic emission prior to rockbursts and earthquakes. Bull Seismol Soc Am 59(3):1259–1279

Bahat D, Rabinovitch A, Frid V (2001) Fracture characterization of chalk in uniaxial and triaxial tests by rock mechanics, fractographic and electromagnetic radiation methods. J Struct 23(10):1531–1547

Benson PM, Vinciguerra S, Meredith PG, Young RP (2008) Laboratory simulation of volcano seismicity. Science 322(5899):249–252

Burlini L, Toro GD (2008) Volcanic Symphony in the Lab. Science 322(5899):207–208

Calder PN, Madsen D (1989) High frequency precursor analysis prior to a rockburst. Int J Rock Mech Min Sci Geomech Abstr 26:3–4

Chen Y (1977) Application of acoustic emission techniques to rock mechanics research. Acta Geophys Sin 4(20):312–321

Chen Y, Yu X (1984) The acoustic emission of rock sample deformation. Chin J Geophys 27(4):392–401

Cleophas TJ, Zwinderman AH (2013) Machine learning in medicine: part two. Springer Netherlands, Berlin, pp 195–206. https://doi.org/10.1007/978-94-007-6886-4_19

Dong LJ, Wesseloo J, Potvin Y, Li XB (2016a) Discriminant models of blasts and seismic events in mine seismology. Int J Rock Mech Min Sci 86:282–291

Dong L, Wesseloo J, Potvin Y, Li X (2016b) Discrimination of mine seismic events and blasts using the fisher classifier, naive bayesian classifier and logistic regression. Rock Mech Rock Engi 49(1):183–211

Dong L, Shu W, Li X, Han G, Zou W (2017) Three dimensional comprehensive analytical solutions for locating sources of sensor networks in unknown velocity mining system. IEEE Access 5(99):11337–11351

Enomoto Y, Hashimoto H (1990) Emission of charged particles from indentation fracture of rocks. Nature 346(16):641–643

Farhidzadeh A, Mpalaskas AC, Matikas TE, Farhidzadeh H, Aggelis DG (2014) Fracture mode identification in cementitious materials using supervised pattern recognition of acoustic emission features. Constr Build Mater 67(2):129–138

Goodfellow SD, Flynn JW, Reyes-Montes JM, Nasseri MHB, Young RP (2014) Acquisition of complete acoustic emission amplitude records during rock fracture experiments. J Acoust Emiss 32:1–11

Gowd TN (1980) Factors affecting the acoustic emission response of triaxially compressed rock. Int J Rock Mech Min Sci Geomech Abstr 17(4):219–223

Haskell NA (1964) Total energy and energy spectral density of elastic wave radiation from propagating faults. Bull Seismol Soc Am 54(6A):1811–1841

He MC, Miao JL, Feng JL (2010) Rock burst process of limestone and its acoustic emission characteristics under true-triaxial unloading conditions. Int J Rock Mech Min Sci 47(2):286–298

He Manchao Z, Fei Z, Shuai YD, Guan L (2015) Feature evolution of dominant frequency components in acoustic emissions of instantaneous strain-type granitic rockburst simulation tests. Rock Soil Mech 36(1):1–8 + 33

Ishida T, Labuz JF, Manthei G, Meredith PG, Nasseri MHB, Shin K et al (2017) ISRM suggested method for laboratory acoustic emission monitoring. Rock Mech Rock Eng 50(3):665–674

Jia X (2013) The eigen spectrum feature of acoustic emission on strain rockburst. China University of Mining & Technology (Beijing), Beijing

Kranz RL (1983) Microcracks in rocks: a review. Tectonophysics 100(3):449–480

Lavrov A (2003) The Kaiser effect in rocks: principles and stress estimation techniques. Int J Rock Mech Min Sci 40:151–171

Li G, Liang Z, Tang C (2015) Morphologic interpretation of rock failure mechanisms under uniaxial compression based on 3D multiscale high-resolution numerical modeling. Rock Mech Rock Eng 48:2235–2262

Li LR, Deng JH, Zheng L, Liu JF (2017) Dominant frequency characteristics of acoustic emissions in white marble during direct tensile tests. Rock Mech Rock Eng 50(5):1337–1346

Liang ZZ, Tang C, Tang S, Xu T, Tao, Zuo YJ (2007) Characteristics of fractal and percolation of rocks subjected to uniaxial compression during their failure process. Chin J Geotech Eng 29(9):1386–1391

Liu JP, Li YH, Xu SD, Xu S, Jin CY, Liu ZS (2015) Moment tensor analysis of acoustic emission for cracking mechanisms in rock with a pre-cut circular hole under uniaxial compression. Eng Fract Mech 135:206–218

Lu C, Dou L, Liu H, Liu H et al (2012) Case study on microseismic effect of coal and gas outburst process. Int J Rock Mech Min Sci 53:101–110

Ma GW, Wang XJ, Ren F (2011) Numerical simulation of compressive failure of heterogeneous rock-like materials using SPH method. Int J Rock Mech Min Sci 48(3):353–363

Mallat SG (1989) A theory for multi- resolution signal decomposition: the wavelet representation. IEEE Trans Pattern Machine Intel 11:674–693

Meng Q, Zhang M, Han L, Pu H, Nie T (2016) Effects of acoustic emission and energy evolution of rock specimens under the uniaxial cyclic loading and unloading compression. Rock Mechanics Rock Engineering 49(10):3873–3886

Mogi K (1962) Study of elastic shocks caused by the fracture of better o-generous material and its relation to earthquake phenomena. Bull of the Earthquake Res Inst, Tokyo, p 40

Moradian Z, Einstein HH, Ballivy G (2016) Detection of cracking levels in brittle rocks by parametric analysis of the acoustic emission signals. Rock Mechanics Rock Engineering 49(3):785–800

Nyquist H (2002) Certain topics in telegraph transmission theory. Proc IEEE 90(2):280–305

Ohnaka M (1976) A physical basis for earthquakes based on the elastic rebound model. Bull Seismol Soc Am 66(2):433–451

Ohtsu M, Tomoda Y, Suzuki T (2007) Damage evaluation and corrosion detection in concrete by acoustic emission. In: Carpinteri A et al (ed) Fracture mechanics of concrete and concrete structuredesign. Assessment and retrofitting of RC structures. Taylor and Francis Group, London

Pei J, Fei W, Liu J (2016) Spatial evolution and fractal characteristics of natural fractures in marbles under uniaxial compression loading based on the source location technology of acoustic emission. Environ Earth Sci 75(9):828

Rodríguez P, Arab PB, Celestino TB (2016) Characterization of rock cracking patterns in diametral compression tests by acoustic emission and petrographic analysis. Int J Rock Mech Min Sci 83:73–85

Sagasta F, Zitto ME, Piotrkowski R, Benavent-Climent A, Suarez E, Gallego A (2018) Acoustic emission energy b-value for local damage evaluation in reinforced concrete structures subjected to seismic loadings. Mech Syst Signal Process 102:262–277

Scholz CH (1968) An experimental study of the fracturing process in brittle rock. J Geophys Res 73(4):1447–1454

Shiotani T (2008) Parameter analysis. In: Grosse C, Ohtsu M (eds) Acoustic emission testing. Springer, Berlin, pp 41–51

Tang CA (1997) Numerical simulation of rock failure and associated seismicity. Int J Rock Mech Min Sci 34(2):249–262

Torresani B (1992) Time-frequency representation: wavelet packets and optimal decomposition. Ann Inst H Poincaré 56(2):215–234

Wang J, Lingzhi Xie H, Xie et al (2016) Effect of layer orientation on acoustic emission characteristics of anisotropic shale in Brazilian tests. J Nat Gas Sci Eng 36:1120–1129

Wieser C, Käsling H, Raith M, Richter R, Moser D, Gemander F, Grosse C, Thuro K (2015) Acoustic emission technique to detect

micro cracking during uniaxial compression of brittle rocks. In: Lollino G et al (eds) Engineering Geology for Society and Territory, vol 6. Springer, Cham, pp 339–341

Wu LX, Geng NG, Wang JH, Cui CY (2000) Remote sensing rock mechanics (RSRM) and associated experimental studies. Int J Rock Mech Min Sci 37(6):879–888

Yangidani T, Ehara S, Teradam (1985) Localization of Dilatancy in Ohshima granite under constant uniaxial stress. J Geophys Res 90(8):6840–6858

Yen GG, Lin KC (2000) Wavelet packet feature extraction for vibration monitoring. IEEE Trans Ind Electron 47(3):650–667

Zhang Z, Zhang R, Xie H, Liu J, Were P (2015) Differences in the acoustic emission characteristics of rock salt compared with granite and marble during the damage evolution process. Environ Earth Sci 73:6987–6999

Zheng W, Wu C (2015) An information processing method for acoustic emission signal inspired from musical staff. Mech Syst Signal Process 66–67:388–398